Turbulence in the human brain: Discovering the homogeneous isotropic functional core organisation of the human brain

Gustavo Deco[1,2,3,4] , and Morten L. Kringelbach[5,6,7]

1. Center for Brain and Cognition, Computational Neuroscience Group, Department of Information and Communication Technologies, Universitat Pompeu Fabra, Roc Boronat 138, Barcelona, 08018, Spain

2. Institució Catalana de la Recerca i Estudis Avançats (ICREA), Passeig Lluís Companys 23, Barcelona, 08010, Spain

3. Department of Neuropsychology, Max Planck Institute for Human Cognitive and Brain Sciences, 04103 Leipzig, Germany

4. School of Psychological Sciences, Monash University, Melbourne, Clayton VIC 3800, Australia

5. Centre for Eudaimonia and Human Flourishing, University of Oxford, UK.

6. Department of Psychiatry, University of Oxford, Oxford, UK

7. Center for Music in the Brain, Department of Clinical Medicine, Aarhus University, DK

Abstract

Turbulence is a special dynamical state driving many physical systems by way of its ability to facilitate fast energy/information transfer across scales. These qualities are important for brain function, but it is currently unknown if the brain also exhibits turbulence as a fundamental organisational principle. Using large-scale neuroimaging data from 1003 healthy participants, we demonstrate both empirically and through the use of a computational whole-brain model that human brain dynamics is organised around a *turbulent homogeneous isotropic functional core*. We show the economy of anatomy of this functional core following the *exponential Markov-Kennedy distance rule* of anatomical connections as a cost-of-wiring principle, which displays a *turbulent-like power scaling law* for functional correlations in a broad spatial range suggestive of a cascade of information processing. Further investigating this, we use the theory of turbulence in coupled oscillators in a whole-brain model to demonstrate that the best fit of our model to the data corresponds to a region of maximally developed amplitude turbulence, which also corresponds to maximal sensitivity to the processing of external stimulations (information capability). This establishes a firm link between turbulence and optimal brain function. Finally, we investigate the contrast between resting and seven tasks, and find the turbulent core in task is similar to that resting state but that the long-distance correlations show task-specific increases. These controlling, symmetry-breaking regions are found in higher-order brain regions outside primary sensory regions. Overall, our results reveal a novel way of analysing and modelling whole-brain dynamics that for the first time ever establishes turbulence as a fundamental basic principle of brain organisation.

Introduction

The study of turbulence remains one of the most exciting unsolved problems of modern physics (*1*). On his death bed, Heisenberg reportedly said, "When I meet God, I am going to ask him two questions: Why relativity? And why turbulence? I really believe he will have an answer for the first". Much progress has been made in the field of fluid and oscillator dynamics in terms of understanding and modelling turbulence (*1-3*). One of the most relevant aspects of turbulence is the ability to facilitate fast energy transfer across in fluids, the statistical study of which was pioneered by Andrey Kolmogorov (*4-6*)). At an abstract level, effective energy transfer can be thought of in terms of efficient information processing. Thus, a key question presents itself, namely is turbulence at the heart of brain dynamics?

Over the last decades, a tremendous amount of research has demonstrated that the core of the functional organisation of the human brain is highly structured in the low dimensional manifold of the so-called resting state networks (*7*). These networks emerge and are shaped by the underlying anatomy (*8*). Recent detailed and exhaustive anatomical research in non-human primates has shown that the anatomical structural core appears to be radically simple, following a homogeneous isotropic rule, namely the exponential Markov-Kennedy distance rule (*9*). This sharpens the fundamental question addressed here, namely whether the functional core of the human brain is turbulent and homogeneous isotropic at the appropriate spatial scale, providing a radically simple basis for resting state networks.

In order to address this fundamental but challenging question, we used Andrey Kolmogorov's phenomenological theory of turbulence (*4, 5*) (see excellent review in (*6*)). This introduced the important concept of *structure functions*, which are based on computing the spatial correlations between any two points in a fluid. He was able to demonstrate a fundamental power scaling law revealing the underlying key mechanisms of fluid dynamics, namely the energy cascades that balance kinetics and viscous dissipation. This spatial power scaling law is a hallmark of turbulence and appears at an intermediate spatial range called the "inertial subrange" where kinetic energy is not dissipated, and merely transferred to smaller scales following Richardson's concept of *cascaded eddies* (*10*) (**Figure 1A**). In that inertial subrange, the *structure functions* show a universal scaling of $r^{2/3}$ and an energy scaling of $k^{-5/3}$, where r is the spatial scale and k the associated wave number of the spectral scale (see **Figure 1B**). Crucially, Kolmogorov demonstrated that at small scales turbulence is homogeneous isotropic and universal. In particular, his approach was very successful in overcoming the severe limitations of inferring macroscopic laws from a pure

constructivist approach based on studying fluid dynamics at the microscopic level described by the Navier-Stokes equations.

We hypothesised that Kolmogorov's approach using structure functions would be useful for neuroscience, especially given that the brain dynamics ultimately come from the spiking behaviour of neurons described by the Hodgkin-Huxley equations, which are a similar set of microscopic differential equations to the Navier-Stokes. Similarly to fluids, a pure constructivist approach is inappropriate for explaining whole-brain brain dynamics (*11*) similar to the situation in turbulence research before Kolmogorov's vital insight. Even more, Kuramoto extended the concept of turbulence from fluids dynamics to the dynamics of coupled oscillators (*2*), demonstrating efficient information processing across scales. The dynamics of the human brain has been described in terms of whole-brain models of similarly coupled oscillators (*8, 12, 13*) but no one has yet investigated whether these dynamics are truly turbulent.

In the following we use a version of Kolmogorov's concept of structure functions to uncover the fundamental principles of brain dynamics at the macroscopic level using large Human Connectome Project (HCP) database with resting state data from 1003 healthy human participants (**Figure 1C**). In order to discover if human brain dynamics are organised around a *homogeneous isotropic functional core*, we use the structure functions on the spatiotemporal fMRI BOLD signals from the HCP resting state data (using the Schaefer parcellation with 1000 parcels, **Figure 1D**). This empirical analysis allowed us to find a *homogeneous isotropic functional core* and *turbulent-like power scaling law* for the average functional correlations in a broad spatial range (examples of the considered functional pairs for a given Euclidean distance are shown in **Figure 1E**).

One thing is to observe, however, and another is to truly understand a phenomenon through a causal mechanistic model. Therefore we used a whole-brain model utilising Stuart-Landau oscillators (*8*) with the structural connectivity determined simply by the exponential Markov-Kennedy anatomy to rigorously demonstrate the fundamental principle of a turbulent core in the brain (**Figure 1F and Figure 1G**). Given that the exponential Markov-Kennedy distance rule is by definition homogeneous isotropic, and that the model shows an excellent fit to the empirical results, this strongly implies that the functional core is homogeneous isotropic.

Finally, in order to find out whether the human brain is indeed turbulent, we applied the insights from coupled oscillators (*2, 3*) to define a local order parameter, representing a spatial average of the complex phase factor of the local oscillators weighted by the coupling (**Figure 1H**). The standard deviation of the modulus of this measure defines the level of amplitude turbulence. Astonishingly, we find that at the dynamical working point of the whole-brain model optimally fitting the empirical data, the system shows maximal *amplitude turbulence*. Even further, we generalised the concept of susceptibility which measures the sensitivity of the brain to the processing of external stimulations, to define a measure of the information capability of the whole-brain model, which captures how different external stimulations are encoded in the dynamics. Remarkably, at the dynamical working point of the model fitting the data where there is maximal amplitude turbulence, we also found maximal information capability. This shows clearly that the human brain does not just follow a turbulent-like power law but that the functional core is genuinely turbulent and this could facilitate optimal information processing across scales, perhaps suggestive of an information cascade.

This functional core is present in the resting state but it is important to investigate whether this core changes when performing cognitive tasks. The HCP dataset contains seven tasks in addition to resting state and so we investigated the core and the long-distance correlations in each of the tasks. We found that the core remained present in tasks and resting state but that the long-distance correlations in symmetry-breaking regions were found in higher-order brain regions outside primary sensory regions.

Overall, our results show that the human brain dynamics are genuinely turbulent, organised around a *homogeneous isotropic functional core* showing turbulent power scaling laws, perhaps reflecting a cascade of efficient information processing across scales.

Results

We applied the fundamental concept of *structure functions* introduced by Kolmogorov in turbulence theory (**Figure 1B**), in order to discover if the human brain obeys similar laws. Here we show how these structure functions reveal a homogeneous isotropic functional core following turbulent-like power scaling law in the human brain. We used a whole-brain model to understand the causal mechanisms underlying this empirical observation. This rigorously demonstrated a

significant fit to the empirical data of a whole-brain model utilising homogeneous isotropic whole-brain anatomical connectivity, ie the exponential Markov-Kennedy distance rule (*9, 14*).

Extending this mechanistic understanding, we then demonstrate that the brain is indeed truly turbulent, showing maximal *amplitude turbulence* at the dynamical working point of the whole-brain model optimally fitting the empirical data. Moreover, at this point of maximal turbulence, we also find maximal information capability, capturing how different external stimulations are encoded in the dynamics. This firmly establishes a strong link between turbulence and optimal brain function.

Exploring the functional core and turbulent-like power law in the empirical data

The empirical data was minimally pre-processed according to the HCP protocol and subsequently filtered in the narrow relevant band between 0.008 and 0.08 Hz, detrended and z-scored (see Methods). We used the Schaefer parcellation with 500 brain regions in each cortical hemisphere (*15*) (**Figure 1D**). For each brain region we compute its precise coordinates in MNI space and the Euclidean distances *r* between any two brain regions (see examples in **Figure 1E**).

We use Kolmogorov's concept of *structure functions* of a variable *u* (in turbulence usually a transversal or longitudinal velocity), which is defined here (and in the Methods) as $S(\mathrm{r}) = \langle (u(\bar{x}+r) - u(\bar{x}))^2 \rangle = 2[B(0) - B(\mathrm{r})]$, where the basic spatial correlations of two points separated by an Euclidean distance *r*, are given by $B(r) = \langle u(\bar{x}+r)u(\bar{x}) \rangle$. Here, we use variable *u* to denote the spatiotemporal fMRI BOLD signals from our analysis of the whole-brain dynamics of the HCP resting state data. The symbol $\langle \quad \rangle$ refers to the average across the spatial location $\bar{x}$ of the nodes and time. Please note that many pairs of nodes across the brain have the same Euclidean distance *r* and are thus averaged in the $\langle \quad \rangle$.

Averaging across participants, **Figure 2A** shows the structure function *S(r)*, plotted in a log-log plot. We clearly observe what could be called an *inertial subrange,* inspired the similar observation in fluid dynamics, where a power law is found (see Kolmogorov's law in **Figure 1B**). Our results show a power scaling law with an exponent of approximately 1/2 in the range between *r*=8.13 and *r*=33.82 in the inertial subrange (shown in the shaded areas in **Figures 2A-C**).

The functional correlation between two nodes, $B(r)$, is computed as a function of the distance between those nodes (averaged across nodes and time), i.e. using homogenous isotropy (see **Figure 2B**). Again, we a power law, here with an negative exponent of approximately -1/2 in the same inertial subrange between *r*=8.13 and *r*=33.82. **Figure 2C** shows as $B(r)$ as function of the distance (in a normal coordinate system) but averaged across time and showing the dispersion across nodes, i.e. all pairs across all participants. This suggests the homogeneity across nodes.

In fact, the homogeneity can be quantified. For each node location $\bar{x}$ for each participant we compute the fitting of the power scaling law in the same inertial subrange, i.e. $\log(B(r)) = a\, log(r) + h$. Here, the parameters a (slope) and h (bias) describe the power scaling law for each participant and each location. **Figure 2D** shows the density distribution (across participants and node locations) of the slope parameter a, while **Figure 2E** shows this for the bias parameter h. Both distributions are unimodal, which is suggestive of a core of homogeneity of the correlation function $B(r)$ across node location. Furthermore, **Figure 2F** shows the density distribution (across participants and node locations) of the mean (across r in the intertial subrange) of the standard deviation of $B(r)$ (labelled isotropy in the figure). This distribution reflects also a unimodal distribution suggestive of isotropy, given that the variability across directions (standard deviation of $B(r)$) is consistent with an isotropic peak.

Fitting the empirical functional data with a whole-brain model

These empirical findings are interesting in terms of demonstrating a homogeneous isotropic functional core, which is following spatial power scaling behaviour in the inertial subrange. However, they are not conclusive given the dispersion and correlative nature of the structure function. Proving that human neuroimaging data observes this fundamental law requires a rigorous causal demonstration with a whole model fitting the empirical data.

So we fitted the functional empirical data using a whole-brain model, constructed using coupled Hopf oscillators at each brain region for emulating the local dynamics (*see Methods*). Whole-brain models link mechanistically the underlying anatomical structure with functional dynamics (*16, 17*). Indeed, the functional global dynamics result from the mutual interactions of local node dynamics coupled through the underlying empirical anatomical structural matrix. Conventionally, this coupling determined by the underlying anatomical connectivity, which is typically created using tractography of diffusion MRI. Here, however, we test the strong hypothesis that the human brain contains a functional homogenous isotropic core following a turbulent-like spatial power law for a given inertial subrange, derived from the exponential Markov-Kennedy distance rule: $\mathrm{C_{np}} =$

$Ge^{-\lambda(r(n,p))}$ (also see Methods). Here C_{np} is the anatomical coupling between brain region *n* and *p*, G is the strength of the coupling and λ is the exponential decay of the connectivity as a function of the distance, i.e. $r(n,p)$, which is simply the Euclidean distance between brain regions.

With this model, we were able to test the hypothesis by studying the root squared error between the empirical and simulated *B(r)* in the inertial subrange as a function of the two free parameters *G* and λ**. Figure 2G** confirms the strong hypothesis that the human brain has a homogeneous isotropic functional core which follows a turbulent-like power law, as clearly seen from the highly significant fit with *G=0.825* and λ=0.24 mm^{-1}. At this optimal point, **Figure 2H** shows the fit between empirical and simulated $B(r)$ for the inertial subrange, with empirical data shown by the red line and standard deviation, while the data from the causal model is shown by the blue line and standard deviation. This causally demonstrates that the human brain contains a homogeneous isotropic functional core, which observes spatial power scaling behaviour in the inertial subrange, generated by the exponential Markov-Kennedy distance rule. Furthermore, this result fits well with the empirical $\lambda = 0.18$ mm^{-1} observed in the anatomy of non-human primates (*9*).

Furthermore, it has been proposed that segregation and integration hold the keys to optimal brain function (*18*). **Figure 2I** shows that at the optimal working point there is optimal balance between segregation and integration. The balance is simply computed as the product of the segregation and integration for the model (*see Methods*). The optimality of balancing segregation and integration at the optimal working point implementing a homogeneous isotropic functional core clearly demonstrates the importance of the underlying fundamental functional organisation of the human brain.

We also demonstrate that the structure function observable constrains the working region of the whole-brain model significantly better than other measures. For example, following the traditional strategy of using the correlation between empirical and simulated functional connectivity matrices is not informative for constraining the model (see **Figure S1**).

Are human brain dynamics turbulent or turbulent-like?

Turbulence has been described not only in fluid dynamics but also as a phenomenon appearing in the dynamics of coupled oscillators (*2*). We wanted to discover if turbulence appears in human brain dynamics and to this end, we studied this problem with a whole-brain model optimally fitting the empirical data. This approach has the advantage to allow us to check for the particular

properties of turbulence at all points in the parameter space of the model and compare this to the parameters optimally fitting the empirical data.

Interestingly, the Markov-Kennedy distance rule is also evident in the empirical HCP dMRI tractography of the human brain. **Figure 3A** shows the fibre densities between the pairs of regions in the Schaefer parcellations as a function of the Euclidian distance between the nodes with blue showing dMRI tractography and red line showing the fitted Markov-Kennedy distance rule. The subpanels show the structural connectivity matrices for the empirical dMRI tractography (left) and the fitted Markov-Kennedy connectivity (right), at the optimal λ=0.18 mm^{-1} for fitting the dMRI connectivity data to the underlying exponential function. These matrices are remarkably similar reflecting the excellent level of fitting.

This fact simplifies the fitting of the same Hopf whole-brain model to the empirical functional data. We built a whole-brain model using the Markov-Kennedy distance rule with λ=0.18 mm^{-1} but included both hemispheres. Thus, we studied the whole brain fit of the root squared error between the empirical and simulated *B(r)* in the inertial subrange as a function of the global coupling parameter *G***.**

In order to rigorously measure turbulence in this whole-brain model, we used the standard definition of a local order parameter, representing a spatial average of the complex phase factor of the local oscillators weighted by the coupling (*3*). True amplitude turbulence can be demonstrated as function of the standard deviation of the modulus of this measure.

As shown in the Methods, we define amplitude turbulence, D, in the same way as shown in (*3*), i.e. we compute standard deviation of the modulus of the local Kuramoto order parameter *R* across time and space. This captures the change in local synchronisation across time and space, as for example demonstrated in **Figure 1H** (based on the findings in (*3*)) showing the space-time evolution of the local synchronisation in the turbulent regime.

Figure 3B shows the evolution of the amplitude turbulence (red line) and the level of model fitting (blue line) as a function of the global coupling parameter, G (see Methods). We find that the amplitude turbulence, D, is increasing with G and reach a plateau until tapering off at high levels.

This means that the model exhibit turbulence at a broad range of global coupling strengths. Remarkably, however, the maximum of amplitude turbulence, D, is found at the optimal working point at $\mathrm{G} = 0.8$, where the model fits the empirical data; specifically $B(r)$, the spatial correlation function of two nodes. The fact that we get a maximum of turbulence at the working point could suggest that the level of turbulence is reflecting the information capabilities of the brain. As an interesting aside, for each value of G, we also measured the goodness of fit of the power law of $B(r)$ in the inertial subrange that we used to show turbulent-like behaviour in the empirical data. **Figure S1** shows that the goodness of fit (red line) only goes below $p<0.05$ for $G>0.65$, which is close to the optimal working point. This is consistent with the findings of high values of amplitude turbulence in the same range and confirms the usefulness of the power-law to capture turbulence. Yet, it is also clear that this measure is not very sensitive to finding optimal turbulence.

We investigated this possibility by defining a measure of *information capability*. To this end, we generalised the concept of *susceptibility*, which is a measure of the sensitivity of the brain to the processing of external stimulations. We define information capability of the whole-brain model, which captures how different external stimulations are encoded in the dynamics. Specifically, we define the *susceptibility* of the whole-brain model as the level of variability of the dynamics over time and space by random perturbations (see Methods). This is easy to implement in our Hopf whole-brain model (*19, 20*), where perturbations can be introduced by changing the local bifurcation parameter $\mathrm{a_n}$ of each brain node n (see Methods). For each value of G, we perturbed the whole-brain model many times (in our case 200 times) with random parameters for the local bifurcation parameter $\mathrm{a_n}$.

Figure 3C shows that the maximum of information capability (red line) is found at G=0.9 which corresponds to the optimal fitting of the whole-brain model to the empirical data (blue line). This clearly demonstrates that maximal turbulence is directly associated with information capability at the working point of the whole-brain model fitting the empirical data and thus presumably reflecting optimal information processing. In contrast, as is shown by the pink line, the simple measure of susceptibility is not maximal at this working point (but high) and in fact does not show a maximum in the shown range of G.

Further probing the question of optimal information processing, we measured the integration and segregation of the whole-brain model in the whole range of global coupling (as before, see

Methods). **Figure 3D** shows the combined measure of segregation/integration (red line) as a function of G. As can be seen the maximum is around the optimal fitting of the whole-brain model to the empirical data (blue line). This suggests the brain is also at its highest level of being able to segregate and integrate information (*18*).

Visualising spatiotemporal patterns of amplitude turbulence in the brain

We have shown the statistics of the amplitude turbulence of the human brain activity but it is instructive to visualise the change over time and space of the local Kuramoto order parameter, R. **Figure 4A** shows the spatiotemporal evolution of amplitude turbulence in empirical data of a single participant in a 2D plot of all 500 parcels in the left hemisphere over the 1200 timepoints. **Figure 4B** shows snapshots for two segments separated in time (the left and right parts marked on the 2D plot) rendered on a flatmap of the hemisphere. In the supplementary material, **Video S1** shows the full spatiotemporal evolution over the full 1200 timepoints of the full resting state session. In order to fully visualise the spatiotemporal evolution of amplitude turbulence, which depends on the synchronisation of neighbouring clusters over time, **Figure 4C** shows a 2D plot of 26 neighbouring parcels running from the front to the back of the brain. Remarkably, the evolution of amplitude turbulence in terms of R closely resembles the typical turbulence found in fluid dynamics and oscillators (compare with (*3*)).

Deeper insights into the spatiotemporal evolution of amplitude turbulence can be gained from studying the whole-brain model for different coupling strengths showing different levels of amplitude turbulence. **Figure 5A** shows 2D plots of the spatiotemporal evolution of the local Kuramoto order parameter, R, reflecting different levels of turbulence in the model for four different coupling strengths (G=0, G=0.4, G=0.8, and G=3.0). Similar to Figure 4, we plot the level of R for all 500 parcels in the left hemisphere over 1200 timepoints. The optimal working point (G=0.8) is highlighted and shows maximal turbulence as can be appreciated by comparing the level of variability of R in the other three 2D plots. Please also note how the uncoupled case (G=0) resembles random spatiotemporal dynamics, while the two cases demonstrate various degrees of turbulence (as shown by the values of D, the variance of R, in Figure 3B). **Figure 5B** shows the corresponding 2D plots of the spatiotemporal evolution of R in 26 neighbouring parcels running from the front to the back of the brain (similar to the plot in Figure 4C). The supplementary material contains four videos (**Videos S2-S5**) of the full spatiotemporal evolution of amplitude turbulence in one hemisphere across the 1200 timepoints of the full resting state session for each G. For the optimal working point fitting the empirical data (G=0.8), **Figure 5C** shows snapshots of for two

segments of separated in time rendered on a flatmap of the hemisphere for each the four values of G. Again, it is remarkable how the spatiotemporal patterns generated by the whole-brain model at for the optimal working point fitting the data (G=0.8) resemble the amplitude turbulence found in the empirical brain activity. It is also clear that there is amplitude turbulence for other values of G, but as shown in **Figure 3B**, the maximal value of turbulence is observed at the working point of the model fitting the empirical data.

Differences between task and resting

The important result that the functional core is the underlying backbone for information processing leaves open the important question of how the turbulent information cascade is controlled when performing different cognitive tasks. To address this crucial question, we studied the seven HCP tasks and contrasted these results with rest.

First, we established a spatial map of the most significant correlations in resting state in order to have this as a reference for the analysis of the tasks. **Figure 6A** shows the group average functional connectivity (FC) correlation matrix for all 1000 parcels across all 1003 participants in the resting state. We calculated the global brain connectivity (GBC) of the FC matrix by calculating the average functional connectivity of each region with all other regions (the mean value of each row across the columns). Right panel of **Figure 6B** shows a rendering of GBC thresholded at the 80% quantile. Remarkably, as shown in **Figure 6C**, there is a strong spatial overlaps with the myelination measured with T1w/T2w (*21, 22*) thresholded at a similar 80% quantile (left subpanel). This can be seen in the middle panel of **Figure 6C**, where GBC is overlaid on spatial myelin map, and in the right panel of the overlapping histograms of the top GBC and top myelin regions as indexed by the spatial location (Schaefer parcellation number), showing a 67.0% overlap. This means that the backbone of resting state processing takes place in primarily visual, auditory and somatomotor regions.

Second, for rest and each task we compare the correlation function B(r) as a function of the distance r. As a representative example, **Figure 6D** shows the contrast between the HCP relational task (red, see Methods) and the resting state (blue), with the shaded error showing the dispersion across nodes, i.e. all pairs across all participants (similar to **Figure 2C**). We have highlighted both the inertial subrange (r=[8.13 33.82] mm, light yellow background) and the long-distance correlation subrange (r>33.82 mm, light grey background). The inertial subrange is mainly unaffected, but the long-distance correlations are significantly increased in the relational task (and all other tasks, not shown). **Figure 6E** shows the histograms of rest (blue) and gambling task (red) of correlations

averaged across the long-distance subrange. As can be seen clearly, the two distributions are significantly different and there is a group of task-specific regions that show larger correlations than the maximum of resting state (which is equally true for the six other HCP tasks, shown in **Figure 7**). **Figure 6F** (left subpanel) shows the spatial maps of the relational task-specific regions are found in higher-order brain regions (in red) and overlaid on the maps for the thresholded GBC map from resting state (in blue). Remarkably the overlap is very low (16.4%) as can be seen in the right panel, which shows the overlapping histograms of the top relational (red) and top GBC (blue) regions as indexed by the spatial location. This finding demonstrates that the task-specific regions are taken from the long-range correlations that serve to control the unaffected turbulent core through symmetry breaking.

Figure 7A shows the same procedure of thresholding the correlations averaged over the long-distance subrange (for the maximum value of the resting state long-distance correlations) applied to all seven HCP tasks (emotion, gambling, working memory (wm), relational, social, language and motor). This is rendered to visualise the task-specific regions for each task, overlaid on the thresholded GBC map from resting state (blue regions). The regions are found in higher-order regions of the frontal, orbitofrontal, parietal, temporal, insular and midline frontal and cingulate cortices.

Importantly, for all tasks there are hardly any overlaps with the resting GBC maps strongly suggestive of significant role of long-distance connections in controlling the unaffected common turbulent core. Interesting, as expected, each of the tasks use different, yet overlapping higher-order regions to perform the relevant cognitive task. We quantified the overlap by computing the intersection between task-specific regions (thresholded at two levels, one at the maximum of GBC and one at the less stringent 99% quantile of the resting state long-distance correlations) (shown in **Figure 7B**). The common regions are compatible with the large literature on higher order functional regions. The common regions are known to engage a network of brain regions in the ventromedial prefrontal/orbitofrontal, insular, mid-cingulate and dorsolateral prefrontal cortices (see **Figure 7B**). We propose that this overlap could correspond to a "cognitive backbone" which is needed to control the turbulent core processing.

Discussion

Overall, we have demonstrated that the functional core of the human brain is turbulent. We used the structure function concept introduced by Kolmogorov in his phenomenological turbulence theory to

show that the empirical resting state data of 1003 HCP participants follows a power scaling law for functional correlations in a broad spatial range suggestive of a turbulent cascade of information processing. The turbulence in human brain data was confirmed using a whole-brain model fitting the empirical data. Using the theory of turbulence in coupled oscillators in a whole-brain model, we rigorously demonstrated that at the best fit of the model to the data, there is maximally developed amplitude turbulence. Furthermore, at this optimal working point, we also find that the brain shows maximal information capability, reflecting optimal sensitivity to the processing of external stimulations. Importantly, this establishes a strong link between turbulence and optimal brain function, which will be important to fully investigate in the coming years and may provide a key to understanding why turbulence is important for optimal human processing and how it may be changed in disease.

Finding a functional core in the empirical data

Human brain activity reflect the underlying brain anatomy (*8*), and this shaping of function by anatomical connectivity gets even stronger in brain states such as deep sleep (*23*) and anaesthesia (*24*). Over the last decades, a large body of convincing research has identified how precisely the underlying anatomical connectivity is responsible for the emergence of the fundamental resting state networks that give rise to the low dimensional manifold of the functional organisation shaped by the human brain (*7*). Even more radical is the proposal that anatomical connectivity of the brain can be described by a structural core following a simple, homogeneous isotropic rule, namely the exponential Markov-Kennedy distance rule that provides the economy of anatomy as a cost-of-wiring principle (*9*). This poses the question of whether the Markov-Kennedy distance rule also gives rise an even more fundamental functional core underlying resting state. To test this, we introduced this law as the basis of our adapted version of Kolmogorov's structure function concept. This was used to study the organisation of the activity in the empirical data from 1003 HCP participants. We found that the data shows turbulent-like power scaling laws in an inertial subrange, confirming that this could be a homogenous isotropic functional core underlying the resting state networks.

Modelling the functional core

Moving beyond correlation, we built a causal mechanistic model using the exponential Markov-Kennedy anatomy to rigorously demonstrate the emergence of a functional turbulent core. The Hopf whole-brain model using the exponential Markov-Kennedy distance rule was able to fit the spatial power scaling law in the inertial subrange of the empirical neuroimaging data. This result

confirms that 1) the exponential Markov-Kennedy distance rule in non-human primates also holds in humans, 2) the existence of a homogenous isotropic functional core, 3) this functional core follows a turbulent-like power-law and that the functional core is likely to underlie the resting state networks. A challenging open question remains the origin of the resting state networks but the present study supports the partial answer given by Kennedy and colleagues, who in their landmark anatomical studies have always stressed that the most relevant connectivity for implementing cognition and higher brain function can be found in the *exceptions* to the exponential Markov-Kennedy distance rule, i.e. long-range connections.

Maximal amplitude turbulence in whole-brain model fitting empirical data

Here, we used the whole-brain Hopf model of coupled oscillators to produce an excellent fit to the empirical data. This allowed us to directly test if the dynamical characteristics of the model follow the established measures of turbulence in coupled oscillators (*2*). Even more, we could explore the model parameters and compare the optimal working point fitting the empirical with all other points in the parameter space to establish that the empirical is maximally turbulent and that this has important functional ramifications, including optimality in information capability and segregation and integration of information.

As shown in the results, we defined a local order Kuramoto parameter which represents a spatial average of the complex phase factor of the local oscillators, weighted by the coupling. Within this framework, amplitude turbulence is defined as the standard deviation of the modulus of this measure (*3*).

The results show maximal *amplitude turbulence* at the dynamical working point of the whole-brain model. This clearly demonstrates that human brain dynamics are turbulent. We also found that this might help the information processing given that we also found maximal information capability of the whole-brain model for capturing how different external stimulations are encoded in the dynamics. Importantly, we also found an optimal balance between segregation and integration at this working point. Taken together this shows clearly that the human brain is genuinely turbulent and this facilitates optimal information processing across scales, suggestive of an information cascade.

Task-specific higher-order regions

We further explored the functional relevance of the exceptions to the Markov-Kennedy distance rule for anatomy. To this end, we contrasted seven cognitive tasks to resting state for all HCP participants. We found that the task-specific functional differences were mainly found in regions in the long-distance subrange of correlations, while the turbulent core in the inertial subrange was mainly unaffected. This means that the turbulent core is essential for basic brain function and reflects the underlying economy of anatomy that keeps the human brain cost effective. Beyond the functional core, higher brain function is achieved through the breaking of the homogeneity and isotropy of the functional core organisation mainly due to the brain networks found in long-distance subrange, which are the functional homologues driven by the anatomical exceptions to Markov-Kennedy distance rule.

Future perspectives

For the first time, using state-of-the-art neuroimaging data from over 1000 people, we demonstrate turbulence in human brain activity, in a tour-de-force technical analysis combining empirical methods and whole-brain modelling adapting established methods from the fields of fluid dynamics and oscillators.

This result significantly expands on previous research aiming at relating spatiotemporal chaos to brain activity (*25-29*). Careful mathematical research has suggested that a main difference between spatiotemporal chaos and turbulence is that the latter is primarily needed for the propagation of disturbances and the transmittal of information from one spatial point to the other (*1, 30*). This could offer a tentative answer not only to Heisenberg's general question of "Why turbulence" but also to the more specific question of why turbulence in the brain. The purpose of turbulence in the brain must be closely linked to catalyse fast and efficient information processing.

The results presented here from our whole-brain modelling of a very large set of empirical human data rigorously confirm that the human brain operates in a turbulent regime showing a maximum of amplitude turbulence and information capability and an optimal balance between integration and segregation.

This new finding of turbulence in the human brain is important for its controllability, not only in directing task activity but more generally for characterising brain states in health and disease (*20,*

31, 32). As such, the findings will allow for much more sensitive and selective biomarkers of brain states and provide important information on how to control brain disorders and find novel, efficient ways to force homeostatic transitions to a healthy state using external perturbations (*33-35*).

Materials and methods

Neuroimaging Ethics

The Washington University–University of Minnesota (WU-Minn HCP) Consortium obtained full informed consent from all participants, and research procedures and ethical guidelines were followed in accordance with Washington University institutional review board approval.

Neuroimaging Participants

The data set used for this investigation was selected from the March 2017 public data release from the Human Connectome Project (HCP) where we chose a sample of 1003 participants. From this large sample we further chose to replicate in the smaller subsample of 100 unrelated participants (54 females, 46 males, mean age = 29.1 +/- 3.7 years). This subset of participants provided by HCP ensures that they are not family relatives, and this criterion was important to exclude possible identifiability confounds and the need for family-structure co-variables in the analyses.

Schaefer parcellation

Schaefer and colleagues created a publicly available population atlas of cerebral cortical parcellation based on estimation from a large data set (N = 1489) (*15*). They provide parcellations of 400, 600, 800, and 1000 areas available in surface spaces, as well as MNI152 volumetric space. We used here the Schaefer parcellation with 1000 areas and estimated the Euclidean distances from the MNI152 volumetric space and extracted the timeseries from HCP using the HCP surface space version.

Neuroimaging acquisition for fMRI HCP

The 1003 HCP participants were scanned on a 3-T connectome-Skyra scanner (Siemens). We used one resting state fMRI acquisition of approximately 15 minutes acquired on the same day, with eyes open with relaxed fixation on a projected bright cross-hair on a dark background as well as data from the seven tasks. The HCP website (http://www.humanconnectome.org/) provides the full details of participants, the acquisition protocol and preprocessing of the data for both resting state and the seven tasks.

Preprocessing and extraction of functional timeseries in fMRI resting data

The preprocessing of the HCP resting state and task datasets is described in details on the HCP website. Briefly, the data is preprocessed using the HCP pipeline which is using standardized methods using FSL (FMRIB Software Library), FreeSurfer, and the Connectome Workbench software (*36, 37*). This preprocessing included correction for spatial and gradient distortions and

head motion, intensity normalization and bias field removal, registration to the T1 weighted structural image, transformation to the 2mm Montreal Neurological Institute (MNI) space, and using the FIX artefact removal procedure (*37, 38*). The head motion parameters were regressed out and structured artefacts were removed by ICA+FIX processing (Independent Component Analysis followed by FMRIB's ICA-based X-noiseifier (*39, 40*)). Preprocessed timeseries of all grayordinates are in HCP CIFTI grayordinates standard space and available in the surface-based CIFTI file for each participants for resting state and each of the seven tasks.

We used a custom-made Matlab script using the ft_read_cifti function (Fieldtrip toolbox (*41*)) to extract the average timeseries of all the grayordinates in each region of the Schaefer parcellation, which are defined in the HCP CIFTI grayordinates standard space. Furthermore, the BOLD time series were transformed to phase space by filtering the signals in the range between 0.008-0.08 Hz and applying the Hilbert transforms in order to obtain the phases of the signal for each brain node as a function of the time.

We computed the functional connectivity (FC) as the correlation between the BOLD timeseries in all 1000 regions in the Schaefer Parcellation. We then computed the global brain connectivity (GBC) as the node-level FC, or node strength, characterizing the average FC strength for each region (*42, 43*). Thus, node strength is defined as $GBC_i = \frac{1}{N}\sum_{j=1}^{N} FC_{ij}$.

The HCP task battery of seven tasks

The HCP task battery consists of seven tasks: working memory, motor, gambling, language, social, emotional, relational, which are described in details on the HCP website (*44*). HCP participants performed all tasks in two separate sessions (first session: working memory, gambling and motor; second session: language, social cognition, relational processing and emotion processing).

Structural connectivity using dMRI

The Human Connectome Project (HCP) database contains diffusion spectrum and T2-weighted imaging data from 32 participants with the acquisition parameters described in details on the HCP website (*45*). The freely available Lead-DBS software package (http://www.lead-dbs.org/) provides the preprocessing which is described in details in Horn and colleagues (*46*) but briefly, the data was processed using a generalized q-sampling imaging algorithm implemented in DSI studio (http://dsi-studio.labsolver.org). Segmentation of the T2-weighted anatomical images produced a white-matter mask and co-registering the images to the b0 image of the diffusion data using SPM12. In each HCP participant, 200,000 fibres were sampled within the white-matter mask. Fibres were

transformed into MNI space using Lead-DBS (*47*). We used the standardized methods in Lead-DBS to produce the structural connectomes for both Schaefer 1000 parcellation Scheme (*15*).

Analysis using Kolmogorov' structure function concept

We adapted Kolmogorov's concept of *structure functions* of a variable *u*, which in turbulence is usually a transversal or longitudinal velocity but here is given by the BOLD signal of the data:

$$S(\mathrm{r}) = \langle (u(\bar{x} + r) - u(\bar{x}))^2 \rangle = 2[B(0) - B(\mathrm{r})] \qquad (1)$$

In Equation 1, the basic spatial correlations of two points separated by an Euclidean distance *r*, given by:

$$B(r) = \langle u(\bar{x} + r) u(\bar{x}) \rangle \qquad (2)$$

where the symbol $\langle \quad \rangle$ refers to the average across the spatial location $\bar{x}$ of the nodes and time.

Whole-brain model

The link between anatomical structure and functional dynamics, introduced more than a decade ago is at the heart of whole-brain network models (*16, 17*). Typically, the anatomy is represented by the structural connectivity (SC) of an individual or average brain, measured in vivo by diffusion MRI (dMRI) combined with probabilistic tractography. The spatial resolution is in the order of 1-2 mm, but with ultra-high field MRI resolutions 0.4 mm can be reached. The structural connectome denotes the wire-diagram of the connections between cortical regions as ascertained from dMRI tractography. The functional global dynamics result from the mutual interactions of local node dynamics coupled through the underlying empirical anatomical SC matrix. Whole-brain models aim to balance between complexity and realism in order to describe the most important features of the brain *in vivo* (*29*). The most successful whole-brain computational models have taken their lead from statistical physics where it has been shown that macroscopic physical systems obey laws that are independent of their mesoscopic constituents. The emerging collective macroscopic behaviour of brain models has been shown to depend only weakly on individual neuron behaviour. This theoretical framework has been successful in explaining the pattern of inter-regional activity correlation measured with fMRI, so called resting-state-networks. Recent developments have shown that whole-brain models are able to describe not only static FC (averaged over all time points), but also dynamical measurements like the temporal structure of the activity fluctuations, the so-called functional connectivity dynamics (FCD) (*8, 48*).

Here, we take the Hopf model and crucially instead of using the underlying anatomy as measured by dMRI tractography, we will assume the homogeneous isotropic *exponential Markov-Kennedy distance rule* derived in exhaustive massive retrograde tract tracing in non-human primates. In other words, assuming this simplified anatomy, we will investigate if the model is able to simulate the empirically measured turbulent-like power law scaling of the correlation function *B(r)*.

The Hopf whole-brain model consists of coupled dynamical units (ROIs or nodes) representing the *N* cortical brain areas from a given parcellation (*8*). For the first analysis, we take the 500 cortical nodes in one hemisphere, while for the subsequent analyses we use the full 1000 cortical nodes in the Schaefer parcellation, as specified in the results. The local dynamics of each brain region is described by the normal form of a supercritical Hopf bifurcation, also known as the Landau-Stuart Oscillator, which is the canonical model for studying the transition from noisy to oscillatory dynamics (*49*). Coupled together with the brain network architecture, the complex interactions between Hopf oscillators have been shown to reproduce significant features of brain dynamics observed in electrophysiology (*50, 51*), MEG (*13*) and fMRI (*20, 34*).

The dynamics of an uncoupled brain region *n* is given by the following set of coupled dynamical equations, which describes the normal form of a supercritical Hopf bifurcation in Cartesian coordinates:

$$\frac{dx_n}{dt} = [a_n - x_n^2 - y_n^2]x_n - \omega_n y_n + \beta\eta_n(t) \quad (3)$$

$$\frac{dy_n}{dt} = [a_n - x_n^2 - y_n^2]y_n + \omega_n x_n + \beta\eta_n(t) \quad (4)$$

where $\eta_n(t)$ is additive Gaussian noise with standard deviation β. This normal form has a supercritical bifurcation a_n=0, so that if a_n>0, the system engages in a stable limit cycle with frequency $f_n = \omega_n/2\pi$. On the other hand, when a_n<0, the local dynamics are in a stable fixed point representing a low activity noisy state. Within this model, the intrinsic frequency ω_n of each region is in the 0.008–0.08Hz band (*n*=1, …, *N*), where *N* is the total number regions.

The whole-brain dynamics was defined by the following set of coupled equations:

$$\frac{dx_n}{dt} = [a_n - x_n^2 - y_n^2]x_n - \omega_n y_n + \sum_{p=1}^{N} C_{np}\left(x_p(t) - x_n\right) + \beta_n\eta_n(t) \quad (5)$$

$$\frac{dy_n}{dt} = [a_n - x_n^2 - y_n^2]y_n + \omega_n x_n + \sum_{p=1}^{N} C_{np}\left(y_p(t) - y_p\right) + \beta_n\eta_n(t) \quad (6)$$

where the noise was fixed β=0.01. The local bifurcation parameters, $a_n = -0.02$, are at the brink of the local bifurcations which is where the best fitting were demonstrated to be achieved. We estimated the intrinsic frequencies from the empirical data, as given by the averaged peak frequency of the narrowband BOLD signals of each brain region. The variable x_n emulates the BOLD signal of each region *n*. To model the whole-brain dynamics we added an additive coupling term representing the input received in region *n* from every other region *p*, which is weighted by the corresponding structural connectivity. In this term, G denotes the global coupling weight, scaling equally the total input received in each brain area. The structural connectivity matrix C_{np} is usually estimated and normalized from dMRI tractography, but here we assume the EDR Markov-Kennedy distance rule, i.e..

$$C_{np} = Ge^{-\lambda(r(n,p))} \tag{7}$$

where $r(n, p)$ is the Euclidean distance between the node n and p. All the measures related to whole-brain model were estimated for each global coupling work point, G, running the simulations a 200 times and averaging the results.

Measure of amplitude turbulence

We measure amplitude turbulence by first defining the Kuramoto local order parameter and then taking the standard deviation of the modulus across time and space (similar to (*3*)). First, we define the amplitude turbulence, $R_n(t)$, as the modulus of the local order parameter for a given brain node as a function of the time:

$$R_n(t)e^{i\vartheta_n(t)} = \sum_p \left[\frac{C_{np}}{\sum_q C_{nq}}\right] e^{i\varphi_p(t)} \tag{8}$$

where $\varphi_p(t)$ are the phases of the BOLD time series and C_{np} the anatomical exponential Markov-Kennedy connectivity matrix (see Equation 7). The BOLD fMRI time series were transformed to phase space by first filtering the signals in the range between 0.008-0.08 Hz and using the Hilbert transforms to extract the evolution of the phases of the signal for each brain node over time (see Methods).

We then measure the amplitude turbulence, D, as the standard deviation across time and space of R:

$$D = \langle R^2 \rangle - \langle R \rangle^2 \tag{9}$$

where the brackets $\langle \quad \rangle$ denotes average across space and time. In order to normalise this measure, we shift D with respect to its value when using a global coupling of G=0, which corresponds to a non-coupled system of oscillators, i.e. random.

Measure of susceptibility

We define the susceptibility of a whole-brain model as the sensitivity of the brain to the processing of external stimulations. We perturb the Hopf whole-brain model at each G by randomly changing the local bifurcation parameter, a_n, in the range [-0.02:0]. We estimate the sensitivity of these perturbations on the spatiotemporal dynamics by measuring the modulus of the local Kuramoto order parameter, i.e. $\tilde{R}_n^{(m)}(t)$ for the perturbed case, and $R_n^{(m)}(t)$ for the unperturbed case. We define susceptibility in the following way:

$$\chi = \langle\langle\langle\tilde{R}_n^{(m)}(t)\rangle_t - \langle R_n^{(m)}(t)\rangle_t)\rangle_{trials}\rangle_s \qquad (10)$$

where $\langle\ \ \rangle_t$, $\langle\ \ \rangle_{trials}$ and $\langle\ \ \rangle_s$ are the mean averages across time, trials and space, respectively.

Measure of information capability

Moving beyond susceptibility, we define the *information capability* of the whole-brain model as a measure to capture how different external stimulations are encoded in the dynamics. Specifically, we perturb the model as above, but here the information capability I is defined as the standard deviation across trials of the difference between the perturbed and unperturbed mean of the modulus of the local order parameter across time, averaged over all brain nodes n, i.e.:

$$\mathrm{I} = \langle\langle(\langle\tilde{R}_n^{(m)}(t)\rangle_t - \langle R_n^{(m)}(t)\rangle_t)^2\rangle_{trials} - \langle(\langle\tilde{R}_n^{(m)}(t)\rangle_t - \langle R_n^{(m)}(t)\rangle_t)\rangle_{trials}^2\rangle_s \qquad (11)$$

where the averages ($\langle\ \ \rangle_t$, $\langle\ \ \rangle_{trials}$ and $\langle\ \ \rangle_s$) are defined as above.

Measure of integration

As a measure of integration we used the mean value of all functional correlation pairs *i* and *j*, i.e.

$$\mathrm{I} = \frac{1}{k}\sum_{i,j>i} F_{ij} = \langle u_i u_j\rangle_t \qquad (12)$$

where k is the number of upper triangular elements in the functional connectivity matrix F, whose elements are defined as the temporal average of the z-scored functional signals u between nodes *i* and j.

Segregation

As a complement of the integration, we used the modularity measure (*52*) as a measure of segregation. Following Rubinov and Sporns (2011), modularity is defined as a measure of the goodness with which a network is optimally partitioned into functional subgroups, i.e. a complete subdivision of the network into non-overlapping modules, and supported by densely connected

network communities. We consider the modularity of our FC matrix. Our measure of modularity is given by,

$$S = \frac{1}{v^+} \sum_{ij} (w_{ij}^+ - e_{ij}^+)\, \delta_{M_i M_j} \qquad (13)$$

Where the total weight, $v^+ = \sum_{ij} w_{ij}^+$, is the sum of all positive or negative connection weights (counted twice for each connection), being $w_{ij}^+ \in (0,1]$ the weighted connection between nodes i and j. The chance-expected within-module connection weights $e_{ij}^+ = \frac{s_i^+ s_j^+}{v^+}$, where the strength of node i, $s_i^+ = \sum_j w_{ij}^+$, is the sum of positive or negative connection weights of i. The $\delta_{MiMj} = 1$ when i and j are in the same module and $\delta_{MiMj} = 0$, otherwise (*53*). For a complete description see (*54*).

Acknowledgements

G.D. is supported by the Spanish Research Project PSI2016-75688-P (AEI/FEDER, EU), by the European Union's Horizon 2020 Research and Innovation Programme under grant agreements n. 720270 (HBP SGA1) and n. 785907 (HBP SGA2), and by the Catalan AGAUR Programme 2017 SGR 1545. MLK is supported by the ERC Consolidator Grant: CAREGIVING (n. 615539), Center for Music in the Brain, funded by the Danish National Research Foundation (DNRF117), and Centre for Eudaimonia and Human Flourishing funded by the Pettit and Carlsberg Foundations.

References

1. M. C. Cross, P. C. Hohenberg, Pattern formation outside of equilibrium. *Reviews of Modern Physics* **65**, 851-1112 (1993); published online Epub07/01/ (10.1103/RevModPhys.65.851).
2. Y. Kuramoto, *Chemical Oscillations,Waves, and Turbulence*. (Springer-Verlag, Berlin, 1984).
3. Y. Kawamura, H. Nakao, Y. Kuramoto, Noise-induced turbulence in nonlocally coupled oscillators. *Physical review. E, Statistical, nonlinear, and soft matter physics* **75**, 036209 (2007); published online EpubMar (10.1103/PhysRevE.75.036209).
4. A. N. Kolmogorov, The local structure of turbulence in incompressible viscous fluid for very large Reynolds numbers. *Proceedings of the USSR Academy of Sciences (in Russian)* **30**, 299-303 (1941).
5. A. N. Kolmogorov, Dissipation of Energy in Locally Isotropic Turbulence. *Proceedings of the USSR Academy of Sciences (in Russian)* **32**, 16-18 (1941).
6. U. Frisch, *Turbulence: The Legacy of A. N. Kolmogorov*. (Cambridge University Press, Cambridge, 1995).
7. J. S. Damoiseaux, S. A. Rombouts, F. Barkhof, P. Scheltens, C. J. Stam, S. M. Smith, C. F. Beckmann, Consistent resting-state networks across healthy subjects. *Proceedings of the National Academy of Sciences of the United States of America* **103**, 13848-13853 (2006); published online EpubSep 12 (10.1073/pnas.0601417103).
8. G. Deco, M. L. Kringelbach, V. Jirsa, P. Ritter, The Dynamics of Resting Fluctuations in the Brain: Metastability and its Dynamical Core [bioRxiv 065284]. *Scientific Reports* **7**, 3095 (2017).
9. N. T. Markov, M. Ercsey-Ravasz, D. C. Van Essen, K. Knoblauch, Z. Toroczkai, H. Kennedy, Cortical high-density counterstream architectures. *Science* **342**, 1238406 (2013); published online EpubNov 1 (10.1126/science.1238406).
10. L. F. Richardson, *Weather prediction by numerical process*. (Cambridge University Press, Cambridge, 1922).
11. Y. Fregnac, Big data and the industrialization of neuroscience: A safe roadmap for understanding the brain? *Science* **358**, 470-477 (2017); published online EpubOct 27 (10.1126/science.aan8866).
12. J. Cabral, H. Luckhoo, M. Woolrich, M. Joensson, H. Mohseni, A. Baker, M. L. Kringelbach, G. Deco, Exploring mechanisms of spontaneous functional connectivity in MEG: How delayed network interactions lead to structured amplitude envelopes of band-pass filtered oscillations. *Neuroimage* **90**, 423-435 (2014); published online EpubDec 7 (10.1016/j.neuroimage.2013.11.047).
13. G. Deco, J. Cabral, M. Woolrich, A. B. A. Stevner, T. Van Hartevelt, M. L. Kringelbach, Single or Multi-Frequency Generators in On-going MEG Data: a Mechanistic Whole-Brain Model of empirical MEG data. *Neuroimage* **152**, 538-550 (2017).
14. N. T. Markov, J. Vezoli, P. Chameau, A. Falchier, R. Quilodran, C. Huissoud, C. Lamy, P. Misery, P. Giroud, S. Ullman, P. Barone, C. Dehay, K. Knoblauch, H. Kennedy, Anatomy of hierarchy: feedforward and feedback pathways in macaque visual cortex. *The Journal of comparative neurology* **522**, 225-259 (2014); published online EpubJan 1 (10.1002/cne.23458).
15. A. Schaefer, R. Kong, E. M. Gordon, T. O. Laumann, X. N. Zuo, A. J. Holmes, S. B. Eickhoff, B. T. T. Yeo, Local-Global Parcellation of the Human Cerebral Cortex from Intrinsic Functional Connectivity MRI. *Cerebral cortex* **28**, 3095-3114 (2018); published online EpubSep 1 (10.1093/cercor/bhx179).
16. G. Deco, V. K. Jirsa, A. R. McIntosh, Resting brains never rest: computational insights into potential cognitive architectures. *Trends in neurosciences* **36**, 268-274 (2013); published online EpubMay (10.1016/j.tins.2013.03.001).
17. G. Deco, M. L. Kringelbach, Great Expectations: Using Whole-Brain Computational Connectomics for Understanding Neuropsychiatric Disorders. *Neuron* **84**, 892-905 (2014).

18. G. Deco, G. Tononi, M. Boly, M. L. Kringelbach, Rethinking segregation and integration: contributions of whole-brain modelling *Nat Rev Neurosci* **16**, 430-439 (2015).
19. G. Deco, J. Cabral, V. M. Saenger, M. Boly, E. Tagliazucchi, H. Laufs, E. Van Someren, B. Jobst, A. Stevner, M. L. Kringelbach, Perturbation of whole-brain dynamics in silico reveals mechanistic differences between brain states. *Neuroimage* **169**, 46-56 (2017); published online EpubDec 7 (10.1016/j.neuroimage.2017.12.009).
20. G. Deco, J. Cruzat, J. Cabral, E. Tagliazucchi, H. Laufs, N. K. Logothetis, M. L. Kringelbach, Awakening: predicting external stimulation forcing transitions between different brain states. *PNAS* **116**, 18088-18097 (2019).
21. M. F. Glasser, D. C. Van Essen, Mapping human cortical areas in vivo based on myelin content as revealed by T1- and T2-weighted MRI. *The Journal of neuroscience : the official journal of the Society for Neuroscience* **31**, 11597-11616 (2011); published online EpubAug 10 (10.1523/JNEUROSCI.2180-11.2011).
22. M. F. Glasser, M. S. Goyal, T. M. Preuss, M. E. Raichle, D. C. Van Essen, Trends and properties of human cerebral cortex: correlations with cortical myelin content. *NeuroImage* **93 Pt 2**, 165-175 (2014); published online EpubJun (10.1016/j.neuroimage.2013.03.060).
23. E. Tagliazucchi, N. Crossley, E. T. Bullmore, H. Laufs, Deep sleep divides the cortex into opposite modes of anatomical-functional coupling. *Brain structure & function* **221**, 4221-4234 (2016); published online EpubNov (10.1007/s00429-015-1162-0).
24. P. Barttfeld, L. Uhrig, J. D. Sitt, M. Sigman, B. Jarraya, S. Dehaene, Signature of consciousness in the dynamics of resting-state brain activity. *Proceedings of the National Academy of Sciences of the United States of America* **112**, 887-892 (2015); published online EpubJan 20 (10.1073/pnas.1418031112).
25. C. van Vreeswijk, H. Sompolinsky, Chaos in neuronal networks with balanced excitatory and inhibitory activity. *Science* **274**, 1724-1726 (1996); published online EpubDec 6 (10.1126/science.274.5293.1724).
26. A. Babloyantz, C. Lourenco, Computation with chaos: a paradigm for cortical activity. *Proceedings of the National Academy of Sciences of the United States of America* **91**, 9027-9031 (1994); published online EpubSep 13 (10.1073/pnas.91.19.9027).
27. W. J. Freeman, Mesoscopic neurodynamics: from neuron to brain. *Journal of physiology, Paris* **94**, 303-322 (2000); published online EpubSep-Dec (10.1016/s0928-4257(00)01090-1).
28. C. J. Honey, R. Kötter, M. Breakspear, O. Sporns, Network structure of cerebral cortex shapes functional connectivity on multiple time scales. *Proceedings of the National Academy of Sciences of the United States of America* **104**, 10240-10245 (2007); published online EpubJun 12 (10.1073/pnas.0701519104).
29. M. Breakspear, Dynamic models of large-scale brain activity. *Nature neuroscience* **20**, 340-352 (2017); published online EpubFeb 23 (10.1038/nn.4497).
30. Y. Oono, C. Yeung, A cell dynamical system model of chemical turbulence. *Journal of Statistical Physics* **48**, 593-644 (1987); published online Epub1987/08/01 (10.1007/BF01019690).
31. S. Gu, R. F. Betzel, M. G. Mattar, M. Cieslak, P. R. Delio, S. T. Grafton, F. Pasqualetti, D. S. Bassett, Optimal trajectories of brain state transitions. *NeuroImage* **148**, 305-317 (2017); published online EpubMar 1 (10.1016/j.neuroimage.2017.01.003).
32. C. Tu, R. P. Rocha, M. Corbetta, S. Zampieri, M. Zorzi, S. Suweis, Warnings and caveats in brain controllability. *NeuroImage* **176**, 83-91 (2018); published online EpubAug 1 (10.1016/j.neuroimage.2018.04.010).
33. M. L. Kringelbach, N. Jenkinson, A. L. Green, S. L. F. Owen, P. C. Hansen, P. L. Cornelissen, I. E. Holliday, J. Stein, T. Z. Aziz, Deep brain stimulation for chronic pain investigated with magnetoencephalography. *Neuroreport* **18**, 223-228 (2007).

34. M. L. Kringelbach, J. Cruzat, J. Cabral, G. M. Knudsen, R. L. Carhart-Harris, P. C. Whybrow, N. K. Logothetis, G. Deco, Dynamic Coupling of Whole-Brain Neuronal and Neurotransmitter Systems. *PNAS*, in press (2020).
35. G. Deco, J. Cruzat, J. Cabral, G. M. Knudsen, R. L. Carhart-Harris, P. C. Whybrow, N. K. Logothetis, M. L. Kringelbach, Whole-brain multimodal neuroimaging model using serotonin receptor maps explains non-linear functional effects of LSD. *Current Biology* **28**, 3065-3074 (2018).
36. M. F. Glasser, S. N. Sotiropoulos, J. A. Wilson, T. S. Coalson, B. Fischl, J. L. Andersson, J. Xu, S. Jbabdi, M. Webster, J. R. Polimeni, D. C. Van Essen, M. Jenkinson, W. U.-M. H. Consortium, The minimal preprocessing pipelines for the Human Connectome Project. *NeuroImage* **80**, 105-124 (2013); published online EpubOct 15 (10.1016/j.neuroimage.2013.04.127).
37. S. M. Smith, C. F. Beckmann, J. Andersson, E. J. Auerbach, J. Bijsterbosch, G. Douaud, E. Duff, D. A. Feinberg, L. Griffanti, M. P. Harms, M. Kelly, T. Laumann, K. L. Miller, S. Moeller, S. Petersen, J. Power, G. Salimi-Khorshidi, A. Z. Snyder, A. T. Vu, M. W. Woolrich, J. Xu, E. Yacoub, K. Ugurbil, D. C. Van Essen, M. F. Glasser, W. U.-M. H. Consortium, Resting-state fMRI in the Human Connectome Project. *NeuroImage* **80**, 144-168 (2013); published online EpubOct 15 (10.1016/j.neuroimage.2013.05.039).
38. T. Navarro Schroder, K. V. Haak, N. I. Zaragoza Jimenez, C. F. Beckmann, C. F. Doeller, Functional topography of the human entorhinal cortex. *eLife* **4**, (2015); published online EpubJun 8 (10.7554/eLife.06738).
39. G. Salimi-Khorshidi, G. Douaud, C. F. Beckmann, M. F. Glasser, L. Griffanti, S. M. Smith, Automatic denoising of functional MRI data: combining independent component analysis and hierarchical fusion of classifiers. *NeuroImage* **90**, 449-468 (2014); published online EpubApr 15 (10.1016/j.neuroimage.2013.11.046).
40. L. Griffanti, G. Salimi-Khorshidi, C. F. Beckmann, E. J. Auerbach, G. Douaud, C. E. Sexton, E. Zsoldos, K. P. Ebmeier, N. Filippini, C. E. Mackay, S. Moeller, J. Xu, E. Yacoub, G. Baselli, K. Ugurbil, K. L. Miller, S. M. Smith, ICA-based artefact removal and accelerated fMRI acquisition for improved resting state network imaging. *NeuroImage* **95**, 232-247 (2014); published online EpubJul 15 (10.1016/j.neuroimage.2014.03.034).
41. R. Oostenveld, P. Fries, E. Maris, J. M. Schoffelen, FieldTrip: Open source software for advanced analysis of MEG, EEG, and invasive electrophysiological data. *Comput Intell Neurosci* **2011**, 156869 (2011)10.1155/2011/156869).
42. M. Demirtas, J. B. Burt, M. Helmer, J. L. Ji, B. D. Adkinson, M. F. Glasser, D. C. Van Essen, S. N. Sotiropoulos, A. Anticevic, J. D. Murray, Hierarchical Heterogeneity across Human Cortex Shapes Large-Scale Neural Dynamics. *Neuron* **101**, 1181-1194 e1113 (2019); published online EpubMar 20 (10.1016/j.neuron.2019.01.017).
43. G. J. Yang, J. D. Murray, X. J. Wang, D. C. Glahn, G. D. Pearlson, G. Repovs, J. H. Krystal, A. Anticevic, Functional hierarchy underlies preferential connectivity disturbances in schizophrenia. *Proceedings of the National Academy of Sciences of the United States of America* **113**, E219-228 (2016); published online EpubJan 12 (10.1073/pnas.1508436113).
44. D. M. Barch, G. C. Burgess, M. P. Harms, S. E. Petersen, B. L. Schlaggar, M. Corbetta, M. F. Glasser, S. Curtiss, S. Dixit, C. Feldt, D. Nolan, E. Bryant, T. Hartley, O. Footer, J. M. Bjork, R. Poldrack, S. Smith, H. Johansen-Berg, A. Z. Snyder, D. C. Van Essen, W. U.-M. H. Consortium, Function in the human connectome: task-fMRI and individual differences in behavior. *NeuroImage* **80**, 169-189 (2013); published online EpubOct 15 (10.1016/j.neuroimage.2013.05.033).
45. K. Setsompop, R. Kimmlingen, E. Eberlein, T. Witzel, J. Cohen-Adad, J. A. McNab, B. Keil, M. D. Tisdall, P. Hoecht, P. Dietz, S. F. Cauley, V. Tountcheva, V. Matschl, V. H. Lenz, K. Heberlein, A. Potthast, H. Thein, J. Van Horn, A. Toga, F. Schmitt, D. Lehne, B. R. Rosen, V. Wedeen, L. L. Wald, Pushing the limits of in vivo diffusion MRI for the

Human Connectome Project. *NeuroImage* **80**, 220-233 (2013); published online EpubOct 15 (10.1016/j.neuroimage.2013.05.078).
46. A. Horn, W. J. Neumann, K. Degen, G. H. Schneider, A. A. Kuhn, Toward an electrophysiological "sweet spot" for deep brain stimulation in the subthalamic nucleus. *Human brain mapping* **38**, 3377-3390 (2017); published online EpubJul (10.1002/hbm.23594).
47. A. Horn, F. Blankenburg, Toward a standardized structural-functional group connectome in MNI space. *NeuroImage* **124**, 310-322 (2016); published online EpubJan 1 (10.1016/j.neuroimage.2015.08.048).
48. E. C. Hansen, D. Battaglia, A. Spiegler, G. Deco, V. K. Jirsa, Functional connectivity dynamics: modeling the switching behavior of the resting state. *NeuroImage* **105**, 525-535 (2015); published online EpubJan 15 (10.1016/j.neuroimage.2014.11.001).
49. Y. A. Kuznetsov, *Elements of applied bifurcation theory*. (Springer, New York, 1998).
50. F. Freyer, J. A. Roberts, R. Becker, P. A. Robinson, P. Ritter, M. Breakspear, Biophysical mechanisms of multistability in resting-state cortical rhythms. *The Journal of neuroscience : the official journal of the Society for Neuroscience* **31**, 6353-6361 (2011); published online EpubApr 27 (10.1523/JNEUROSCI.6693-10.2011).
51. F. Freyer, J. A. Roberts, P. Ritter, M. Breakspear, A canonical model of multistability and scale-invariance in biological systems. *PLoS computational biology* **8**, e1002634 (2012)10.1371/journal.pcbi.1002634).
52. M. Rubinov, O. Sporns, Weight-conserving characterization of complex functional brain networks. *Neuroimage* **56**, 2068-2079 (2011); published online EpubJun 15 (10.1016/j.neuroimage.2011.03.069).
53. M. E. Newman, Modularity and community structure in networks. *Proceedings of the National Academy of Sciences of the United States of America* **103**, 8577-8582 (2006); published online EpubJun 6 (10.1073/pnas.0601602103).
54. O. Sporns, *Networks of the Brain*. (The MIT Press, 2010), pp. 423.

Figures

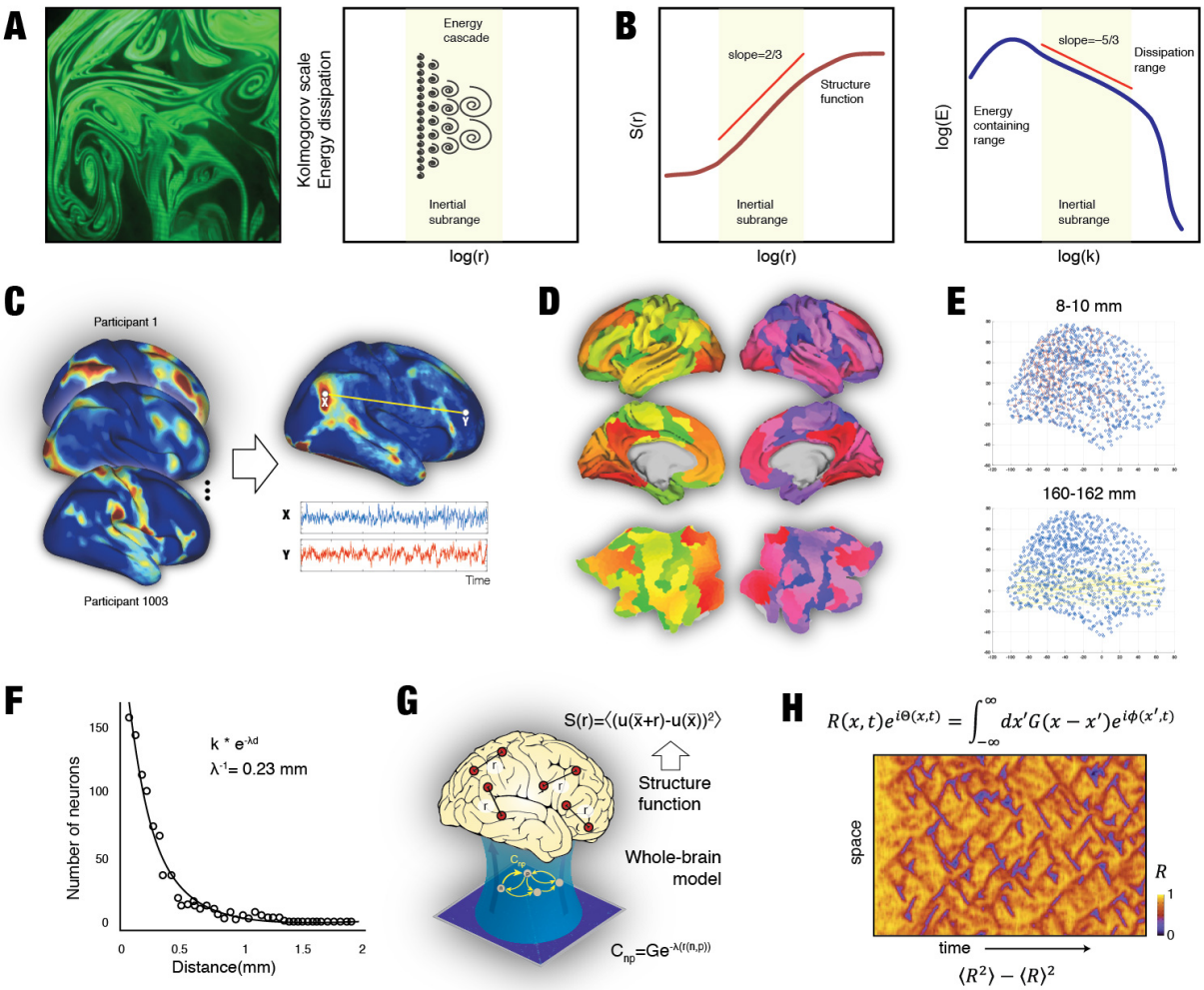

Figure 1. Measuring turbulence in human brain activity. A) *Kolmogorov's phenomenological theory of turbulence is based on the concept of structure functions. In turn, this was inspired by Richardson's concept of cascaded eddies. The left panel shows a snapshot of turbulence in a real physical system with different sizes of eddies, whose hierarchical organisation is schematised for the inertial subrange in the right panel.* ***B)*** *Power laws are found in an inertial subrange where the structure functions show a universal scaling of* $r^{2/3}$ *(left panel) and an energy scaling of* $k^{-5/3}$ *(right panel), where r is the spatial scale and k the associated wave number of the spectral scale. This power law behaviour reflects the energy transfer cascade found in turbulence.* ***C)*** *Here, to detect the presence of turbulence in human brain activity, we used state-of-the-art resting state data from a large set of 1003 healthy human participants in the Human Connectome Project (HCP) database.* ***D)*** *We extracted the timeseries from each the 1000 parcels in the fine-grained Schaefer parcellation, here shown as slices in MNI space and on the surface of the HCP CIFTI space.* ***E)*** *The function structure is based on the functional correlations between pairs with equal Euclidean distance, r, in MNI space. Here we show two examples of the pairs with r=8-10mm (top) and*

r=160-162mm (bottom). ***F)*** *It has been that most of the underlying brain connectivity follows the exponential decay described by the exponential Markov-Kennedy distance rule. The figure shows the number of connected neurons as a function of distance based on a massive tract tracing studies in non-human primates.* ***G)*** *Here, we used this anatomical basis in a whole-brain model based on Stuart-Landau oscillators (8) aiming to establish the causal mechanisms underlying for the emergence of a functional homogeneous isotropic core showing turbulence.* ***H)*** *Our analysis and whole-brain modelling used Kuramoto's rigorous definition of turbulence for coupled oscillators, where he defines a local order parameter, representing a spatial average of the complex phase factor of the local oscillators weighted by the coupling. The standard deviation of the modulus of this measure defines the level of amplitude turbulence, here shown for a ring of Stuart-Landau oscillator system (3).*

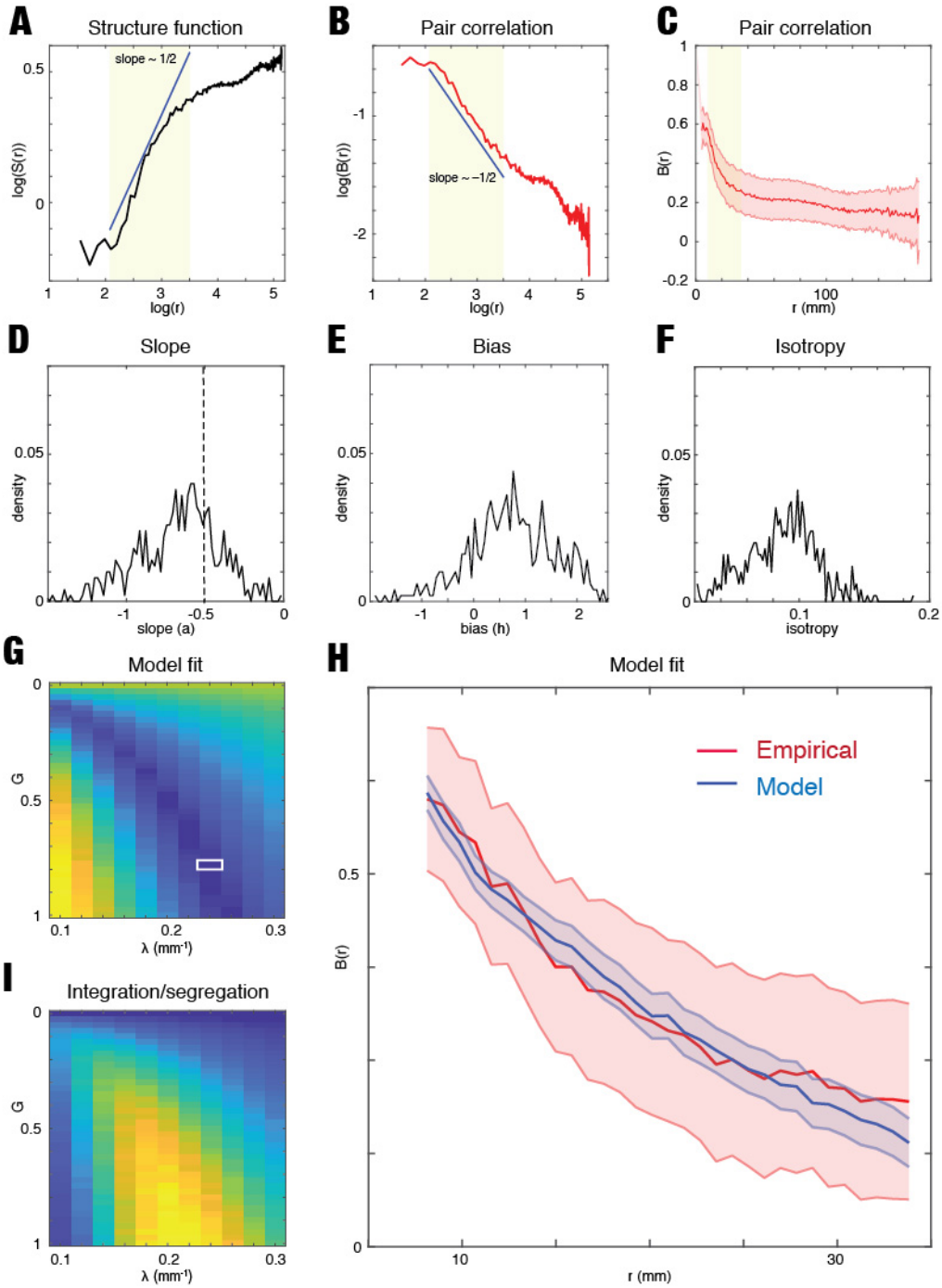

Figure 2. Discovering the turbulent homogeneous isotropic core functional organisation of the human brain. A) *Spatial power scaling law of the structure function S(r) as a function of log(r) in human neuroimaging data of 1003 participants for the correlation function.* ***B)*** *Same spatial power scaling law for the correlation B(r) as a function of log(r).* ***C)*** *The correlation function B(r) as a function of the distance r, but showing the dispersion across regions.* ***D)*** *The unimodal density distribution (across participants and node locations) of the slope parameter* a. ***E)*** *Similar unimodal density distribution of the bias parameter* h. ***F)*** *Unimodal density distribution of the mean (across r in the inertial subrange) of the standard deviation of B(r). These distributions strongly suggest a core of homogeneous isotropic function.* ***G)*** *The results of modelling provide causal support for our*

hypothesis that the human brain contains a functional homogenous isotropic core following a turbulent-like spatial power law for a given inertial subrange. We show the root squared error between the empirical and simulated B(r) in the inertial subrange as a function of the two free parameters G and ***λ.*** *This finds a perfect fit with G=0.825 and λ=0.24 mm*$^{-1}$. ***H)*** *For these optimal parameters, we plot the remarkable fit between empirical and simulated B(r) for the inertial subrange.* ***I)*** *At the optimal parameters, we show an optimal balance between integration and segregation, computed as their product (see Methods).*

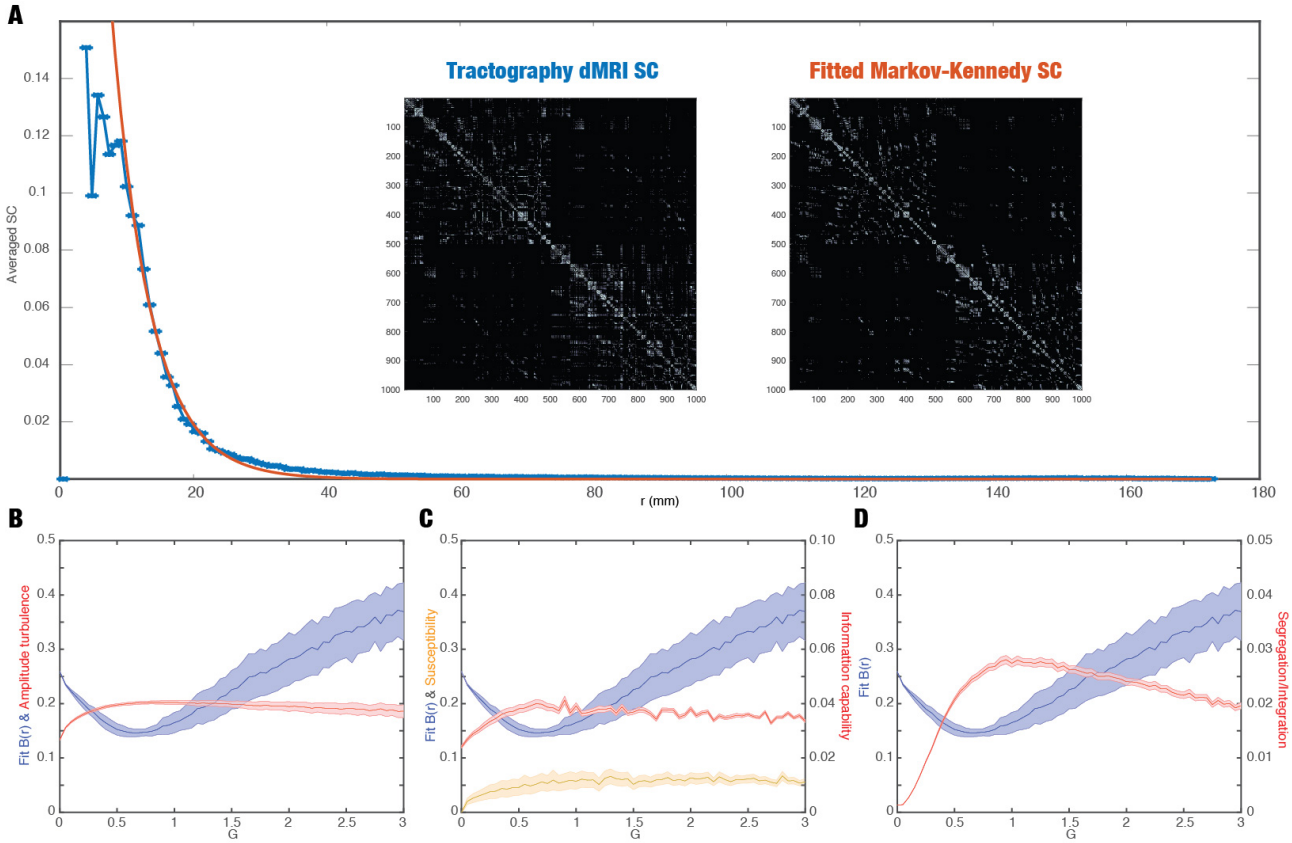

Figure 3. Whole-brain modelling demonstrating turbulence in the empirical data. A) *The Markov-Kennedy distance rule is also evident in the empirical HCP dMRI tractography of the human brain, as shown by the fibre densities between the pairs of regions in the Schaefer parcellations as a function of the Euclidian distance between the nodes with blue showing dMRI tractography and red line showing the fitted Markov-Kennedy distance rule at the optimal* λ*=0.18* mm^{-1}*. The remarkable similarity can be appreciated by comparing the two subpanels. On the left is shown the structural connectivity matrices for the empirical dMRI tractography and on the right the optimally fitted Markov-Kennedy connectivity, which was used as the basis for the whole-brain model.* ***B)*** *The figure shows the whole brain fit of the root squared error between the empirical and simulated B(r) in the inertial subrange as a function of the global coupling parameter G (black). The model shows amplitude turbulence (red line, defined in Methods) in a broad range of G but maximal amplitude turbulence is found at the optimal working point fitting the data (*$G = 0.8xx$*).* ***C)*** *The maximal amplitude turbulence is likely to reflect an optimal level of information processing, which we quantify in a measure of information capability, a meaningful extension of the standard concept of susceptibility (see Methods). As can be seen the maximum of information capability (red line) is found at G=0.8 which corresponds to the optimal fitting of the whole-brain model to the empirical data (black line) and maximal amplitude turbulence. In contrast, the simple measure of susceptibility (orange line) is high but not maximal at the working point.* ***D)*** *Interestingly at the optimal point where the whole-brain model fits the empirical data (black line) and shows maximal*

amplitude turbulence and information capability, we also find an optimal balance between segregation/integration (red line) as a function of G.

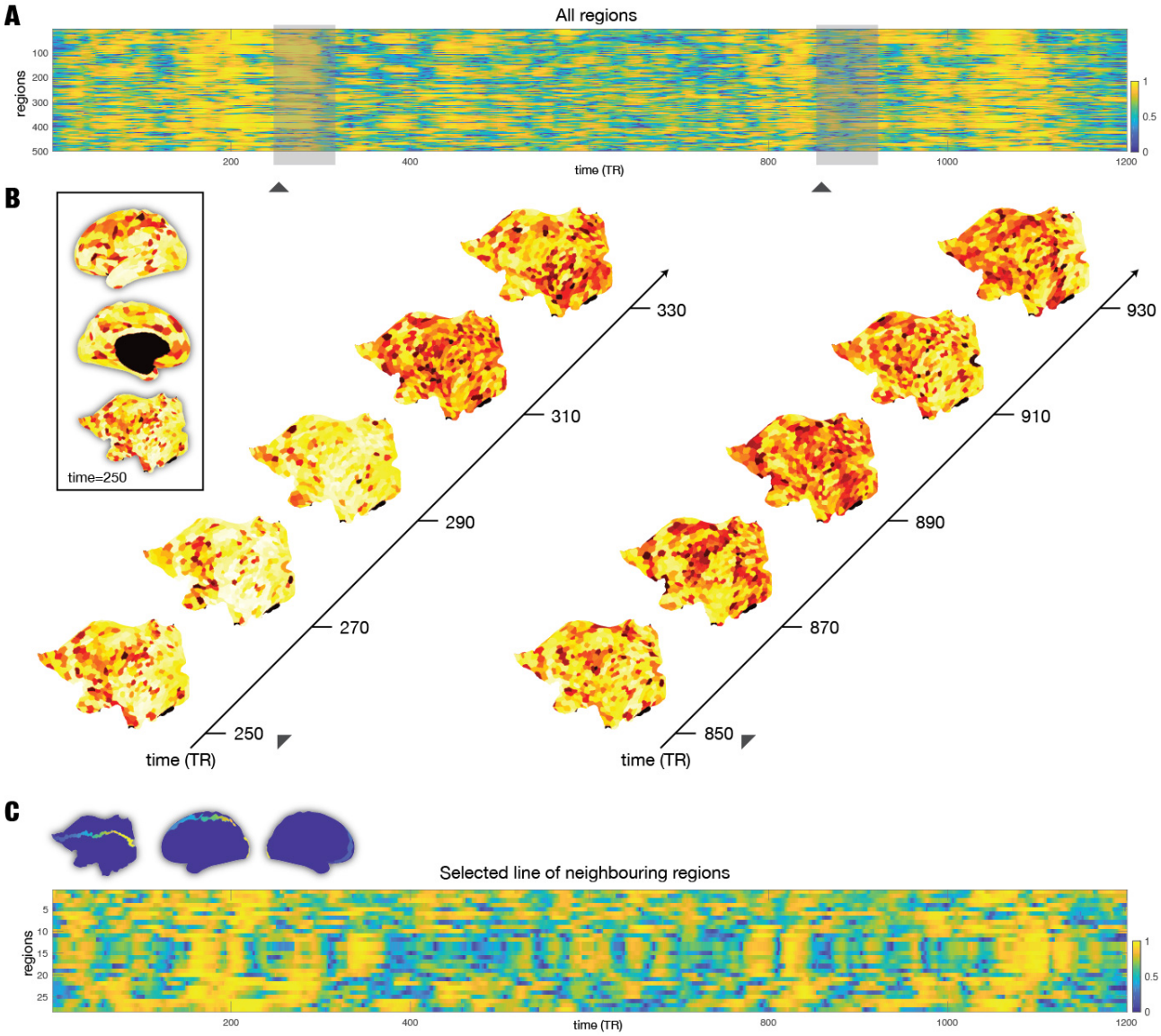

Figure 4. Spatiotemporal evolution of amplitude turbulence in empirical data. A) *The figure visualises the change over time and space of the local Kuramoto order parameter, R, reflecting amplitude turbulence in a single participant. Amplitude turbulence can be clearly seen in the 2D plot of all 500 parcels in the left hemisphere over the 1200 timepoints.* ***B)*** *This can be appreciated from the continuous snapshots for two segments separated in time (left and right parts) rendered on a flatmap of the hemisphere (see insert with renderings of a single snapshot on the inflated and flatmapped cortex). Furthermore, the full spatiotemporal evolution can be appreciated in the video (found in the supplementary material,* ***Video S1****) over the full 1200 timepoints of the full resting state session.* ***C)*** *The synchronisation of clusters over time is dependent on the neighbourhood and so to further visualise the spatiotemporal evolution of amplitude turbulence, we show a 2D plot of 26 neighbouring parcels running from the front to the back of the brain (see blue insert).*

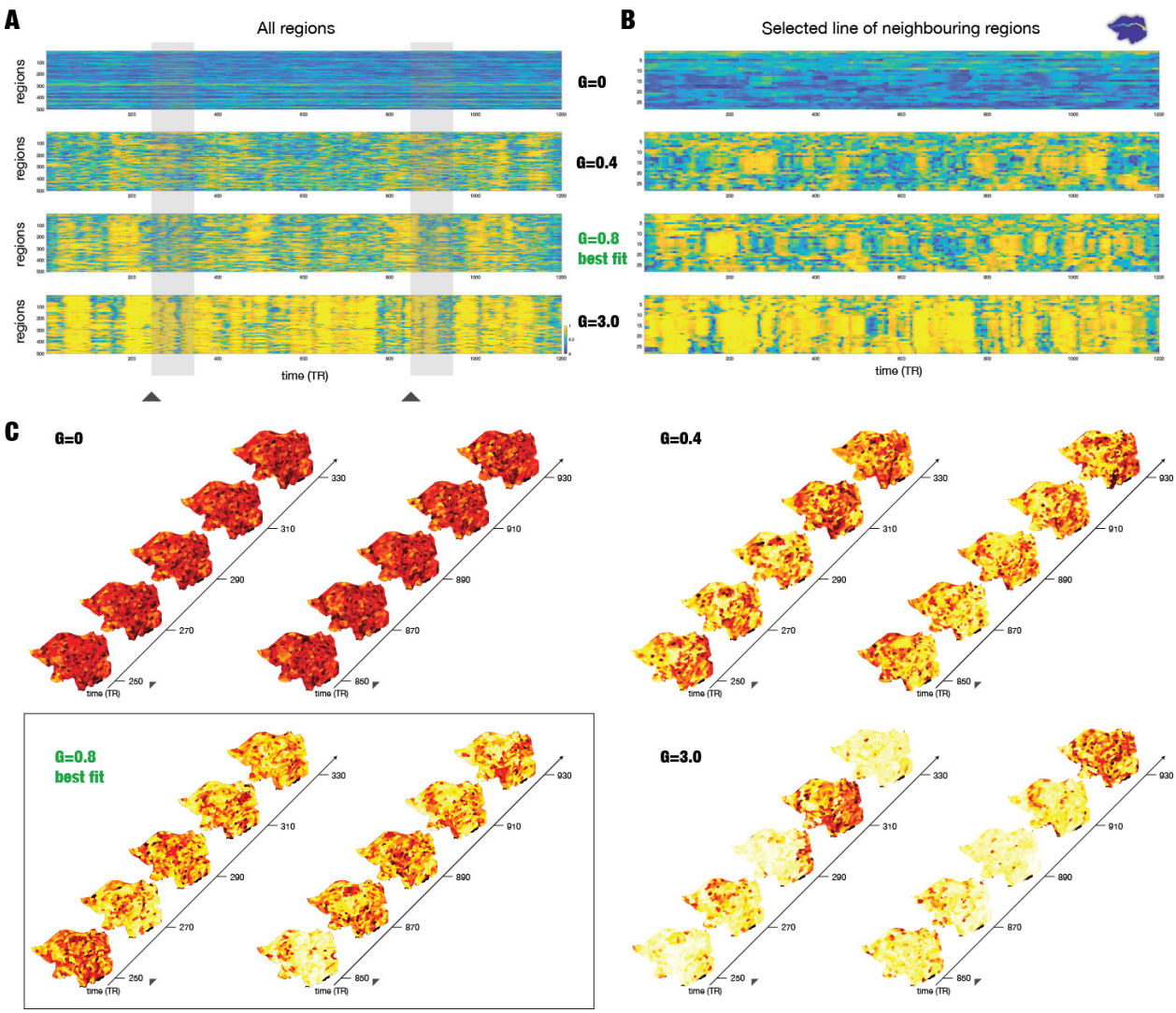

Figure 5. The spatiotemporal evolution of whole-brain model for different coupling strengths showing different levels of amplitude turbulence. A) *For four different coupling strengths (G=0, G=0.4, G=0.8, and G=3.0), we show a 2D plot of the spatiotemporal evolution of the local Kuramoto order parameter, R, reflecting different levels of turbulence in the model (for all 500 parcels in the left hemisphere over 1200 timepoints). The highlighted optimal working point (G=0.8 in red) is showing maximal turbulence as can be appreciated by comparing to the other three 2D plots.* ***B)*** *Similar to Figure 4C, for all four values of coupling strengths, G, we show 2D plots of the spatiotemporal evolution of amplitude turbulence in 26 neighbouring parcels running from the front to the back of the brain.* ***C)*** *Similarly, we show continuous snapshots for two segments of the model at G=0, G=0.4, G=0.8, and G=3.0, separated in time (left and right parts) rendered on a flatmap of the hemisphere. Furthermore, the full spatiotemporal evolution of each can be appreciated in the videos for each G (found in the supplementary material,* ***Videos S2-S5****) over the full 1200 timepoints of the full resting state session.*

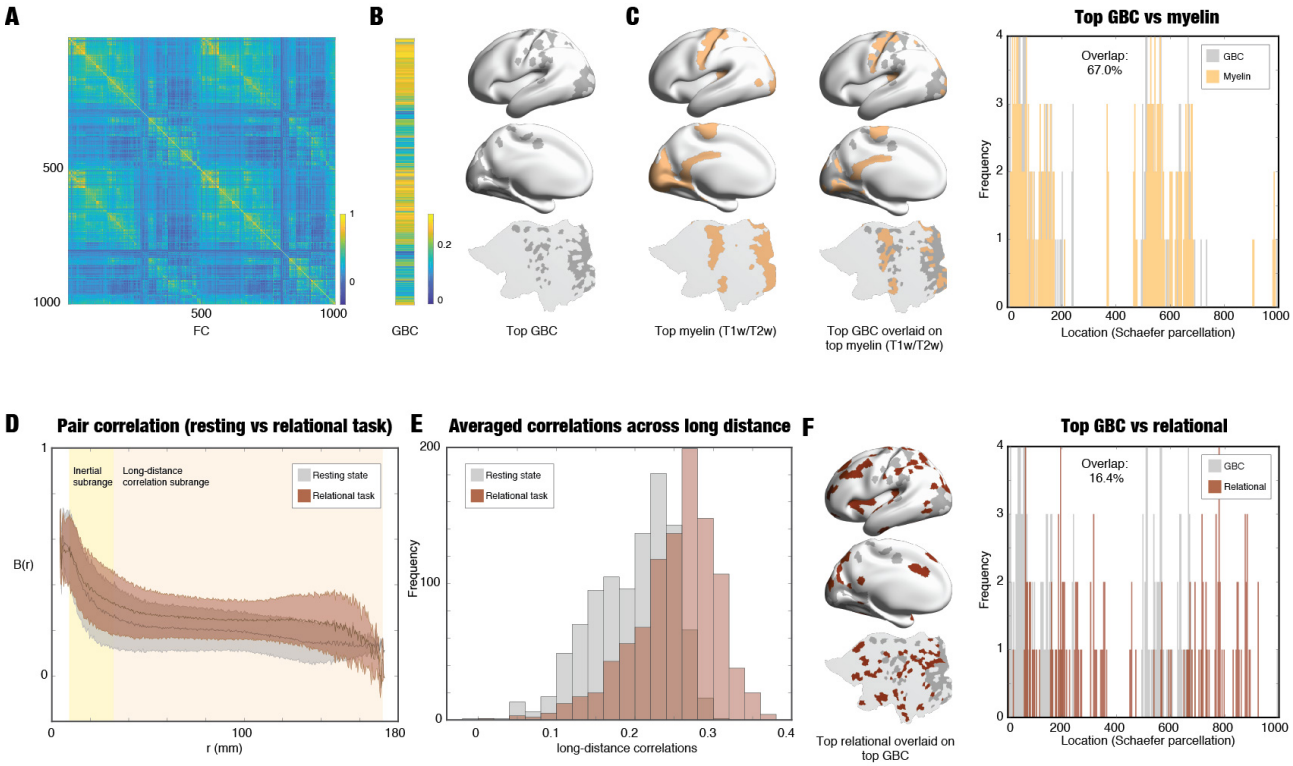

Figure 6. Discovering the functional exceptions driving the turbulent core in cognitive tasks. A) *The figure shows the functional connectivity in resting state between the 1000 regions in the Schaefer1000 parcellation averaged across all HCP 1003 participants.* ***B)*** *Similarly, from this we computed the global brain connectivity (GBC) as the mean correlation between each region with the rest of the brain (42) which characterises the node-level connectivity. The left panel shows the GBC vector (averaged over all participants) while the right panel shows a rendering on the brain of position of the top 20% quantile GBC regions. The top part shows them rendered on the left hemisphere, the middle part the midline while the bottom part shows a rendering on a flat map of the left hemisphere.* ***C)*** *The left panel shows the top regions with myelination (T1w/T2w) rendered on the brain. As can be seen in the middle panel, there is a strong spatial overlap between the top GBC regions and the top regions with myelination. This can also be seen in the right panel of the overlapping histograms of the top GBC and top myelin regions as indexed by the spatial location (Schaefer parcellation number), which shows a 46.5% overlap.* ***D)*** *Example of the pipeline finding the functional exceptions applied to HCP relational task (see Methods). Here is shown the contrast between the relational task (red) and the resting state (blue), with the shaded error showing the dispersion across nodes, i.e. all pairs across all participants. The inertial subrange (r=[8.13 33.82] mm) is highlighted with a light yellow background, while the long-distance correlation subrange (r>33.82 mm) is shown on a light grey background. As can been clearly seen, the long-range correlations are mainly increased in task, whereas the inertial subrange correlations remain unchanged.* ***E)*** *We show a histogram of the difference of the average correlation for each spatial*

location across the long-distance subrange. The histogram for task (in red) is clearly showing higher correlations than the histogram for resting (in blue). F) We found the most changed long-distance regions in the relational task by thresholding the pair correlation by the maximum pair correlation of the resting condition. The left panel shows a rendering of the top changing regions in the relational task overlaid on the top GBC regions. The overlap is very low (18.2%) as can be seen in the right panel, which shows the overlapping histograms of the top relational (red) and top GBC (blue) regions as indexed by the spatial location. This is strong evidence that the most changed regions in task are complementary to the unchanged fundamental resting GBC regions.

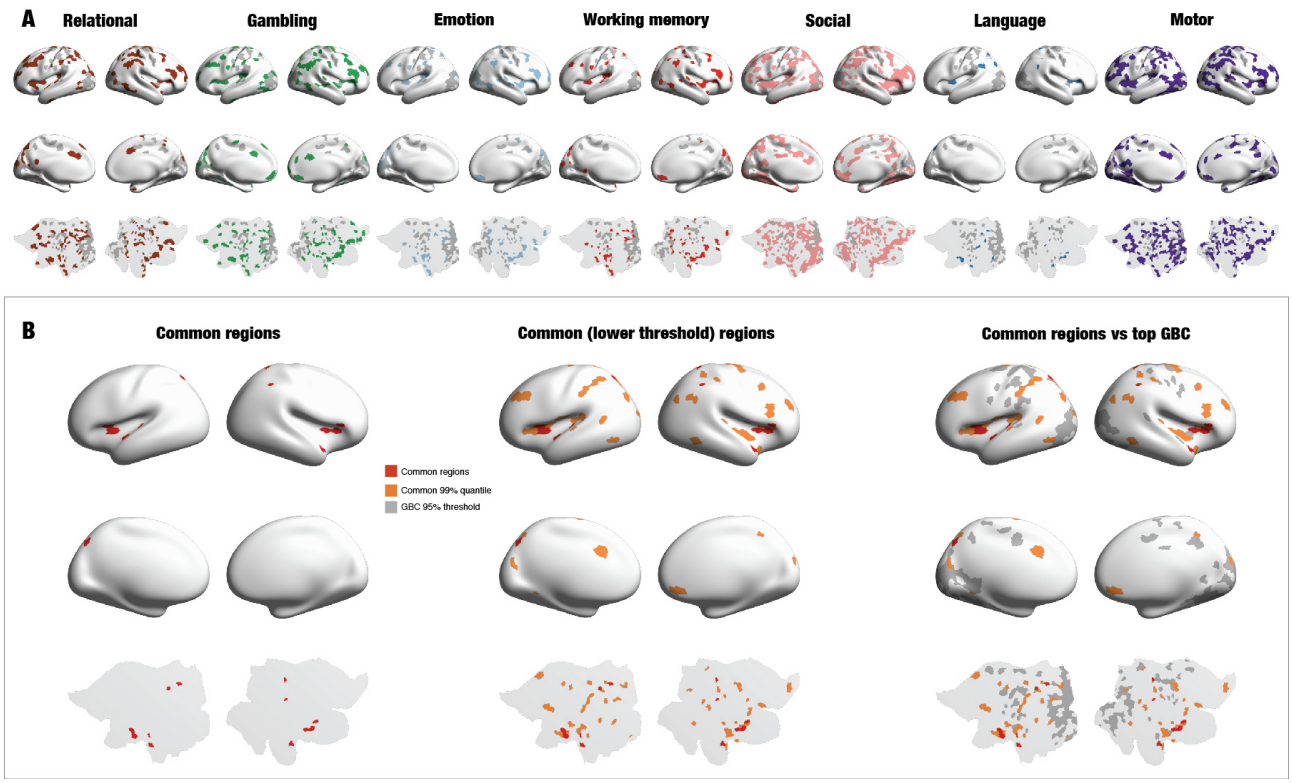

Figure 7. Comparing task-specific exceptions across seven tasks. ***A)*** *The same pipeline shown in Figure 6 was applied to all seven HCP tasks (relational, gambling, emotion, working memory (wm), social, language and motor). These are rendered on side views, midline views and flat map of the left hemisphere to visualise the task-specific regions for each task, overlaid on the thresholded GBC map from the resting state (dark blue).* ***B)*** *The overlap of task-specific exceptions is quantified by computing the intersection between task-specific regions by thresholding of the seven tasks at two thresholds: max (leftmost panel, red) and 99% quantile (middle panel, orange) of the resting state long-distance correlations). These are then overlaid on the GBC map (right panel, grey). This overlap could correspond to a "cognitive backbone" which is needed to control the turbulent core processing.*

Supplementary Figures

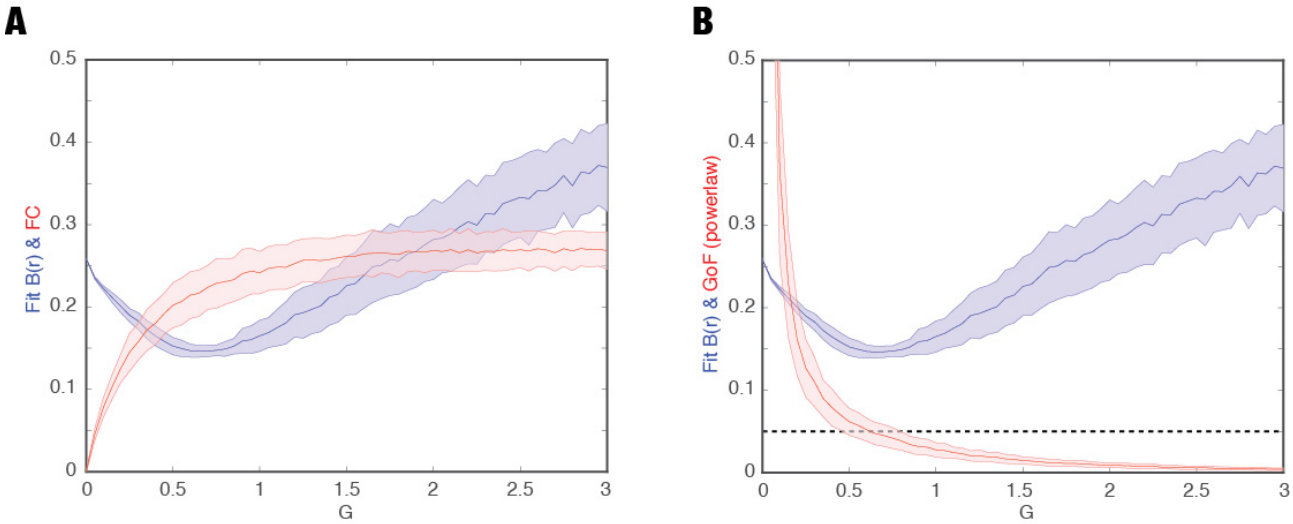

Figure S1. Additional fitting strategies. A) The traditional strategy of fitting using the correlation between empirical and simulated functional connectivity matrices (red line) is not informative for constraining the model. B) The power law fitting of the pair correlation function B(r) in the inertial subrange (information cascade) can also be useful for capturing turbulence but is not very sensitive to finding optimal turbulence. The goodness of fit (red line) only goes below $p<0.05$ for $G>0.65$, which is evidence for the existence of power law. This is consistent with the findings of high values of amplitude turbulence in the same range.

Supplementary Videos S1-S5. Spatiotemporal evolution of amplitude turbulence in empirical and simulated data. *The videos visualise the change over time and space of the local Kuramoto order parameter, R, reflecting amplitude turbulence in the brain. The videos show the inflated 3D side and midline views as well as flat maps of the hemispheres over the 1200 timepoints of the full resting state session. Video S1 shows the empirical data from a representative single participant, while Videos S2-S5 show the amplitude turbulence for four different values of the global coupling G in the whole-brain model (G=0.8 [optimal], G=0, G=0.4, G=3.0).*